Bayesian and Least Squares Approaches to Ultrasonic Scatterer Size Image Formation

Pawan Chaturvedi, *Member, IEEE*, and Michael F. Insana, *Member, IEEE*

Abstract—Scatterer size images can be used to describe renal microstructure and function *in vivo*. Such information may facilitate early detection of disease processes. When high range resolution is required, however, it is necessary to analyze short data segments. Periodogram-based maximum likelihood (ML) techniques for scatterer size estimation are limited in these situations by noise and range-gate artifacts. Moreover, when the input signal-to-noise ratio (SNR) of the echo signal is small, performance is further degraded. If accurate prior information about the approximate properties of the object is available, it can be incorporated into the solution to improve the estimates by reducing the number of possible solutions. In this paper, use of prior knowledge in scatterer size image formation is investigated. A maximum *a posteriori* (MAP) estimator, based on a random-object model, and an iterative constrained least squares (CLS) estimator, based on a deterministic-object model, are designed. Their performances and that of a Wiener filter are compared with the ML technique as a function of gate duration and SNR.

I. Introduction

QUANTITATIVE ultrasonic analysis of biological tissues provides histological information that is not available with other non-invasive techniques. Scatterer size estimates, in particular, have demonstrated an ability to quantify important properties of tissue microstructure and function, *in vivo*. For example, measurements of temporal variations in scatterer size for a fixed tissue volume [1],[2],[3],[4] and images of spatial variations in scatterer size size at a given time [5],[6],[7] offer new opportunities for studying disease processes. If these ultrasonic methods can be developed into sensitive diagnostic tools, it may be possible to analyze histological features non-invasively.

The relationships between acoustic measurements and the microstructure of biological tissues are beginning to be understood [8],[9],[10]. However, it is the sensitivity of scatterer size estimates to changes in tissue microstructure that will ultimately determine the diagnostic utility of this approach. The challenge for scatterer size imaging is to suppress the noise and yet maintain contrast and spatial resolution sufficient to accomplish the diagnostic task.

P. Chaturvedi and M. F. Insana are with the Department of Radiology, University of Kansas Medical Center, Kansas City, KS 66160–7234 (e-mail: pawan@research.kumc.edu and insana@research.kumc.edu).

Visualizing targets in scatterer size images is sometimes difficult [6] because tissues are random scattering media; the coherent detection process produces speckle and reduces the time-bandwidth product. For example, 1–8 mm range resolution is typical of a scatterer size image formed in a C-scan plane from a volume set of echo data [11]. To estimate the scatterer size, the frequency spectrum of each short-time waveform segment is analyzed independently. Therefore, shorter waveform segments provide fewer independent data samples in a fixed measurement bandwidth, increasing the variance of scatterer size estimates [12]. Consequently, periodogram-based maximum likelihood (ML) estimation techniques, such as those described by us previously [11], generate noisy scatterer size images. In the present study, we explore the possibility of improving the detectability of scatterer size images by reducing noise through the use of prior information about the object being imaged.

Histological data from the literature provides the necessary information for many normal and diseased organ systems. For example, in studying renal diseases, it is known that the average glomerular size in a normal human is approximately 210 μm [13], and that glomeruli undergo hypertrophy at the onset of sclerosis [14]. Although the accuracy of the quantitative data in different applications is variable, we will show that even the most basic prior information improves image quality. To demonstrate the improvement, we study a known object and define performance of the imaging system in terms of a contrast-to-noise ratio (CNR).

Prior information is included in the estimation process in two ways, depending on the nature of the object studied. In both cases, measured data are modeled as a linear function of the object. The first approach is to consider the object as stochastic [15],[16],[17]. Bayesian estimation techniques form solutions that include information about the object known prior to the measurement. Specifically, the maximum *a posteriori* (MAP) approach is considered in this work. The second approach is to consider the object as deterministic [18],[19],[20],[21]. A least-squares algorithm provides solutions that are constrained by the prior information about the object. This is the well-known constrained least-squares (CLS) approach to parameter estimation. MAP and CLS techniques both reduce to the ML solution when confidence in the prior knowledge is low.

The following section summarizes the model of echo-data formation that is the basis for the MAP and CLS techniques. Details of the model are described in [12].

II. MEASUREMENT MODEL

The measurement vector $\mathbf{x}^t = \{x[0], x[1] \ldots x[m] \ldots [N-1]\}$ is a time sequence of data samples recorded during a pulse-echo experiment. (Row vector $\mathbf{x}^t$ is the transpose of column vector $\mathbf{x}$.) We use the notation, $X(k) = \mathcal{F}\{x[m]\} = \sum_{m=0}^{\infty} x[m] \exp(-imkc\Delta t)$ to indicate a discrete-time Fourier transform of $\mathbf{x}$, where Δt is the sampling interval, c is the speed of sound, $k = 2\pi f/c$ is spatial frequency, and f is temporal frequency. The measured frequency response $X(k)$ is modeled as a tissue response function $R(k)$ that has been filtered by the sensitivity function $H(k)$ according to the linear model [29],

$$X(k) = H(k)R(k) + N(k) \ , \tag{1}$$

where $N(k)$ is the Fourier transform of a zero mean, white, Gaussian noise process with variance σ_n^2. We use the notation $\mathcal{N}(0, \sigma_n^2)$ to indicate this Gaussian process.

The tissue function $R(k)$ describes the spatial distribution of tissue scattering sites, and therefore is of principal interest in scatterer size estimation. The average scatterer size D represents the characteristic dimension of the microanatomy that scatters ultrasound in the frequencies within the measurement bandwidth. The relationship between $R(k)$ and D is given by

$$E\{R(k)\} = \exp\left(-k^2 D^2/3.11^2\right) \ , \tag{2}$$

This model for $R(k)$ was selected to yield the acoustic form factor $F(k) = E\{|R(k)|^2\}$ observed experimentally for renal tissues [8],[11].

$H(k)$ defines the sensitivity of the measurement spectrum to the tissue function at each k. For a Gaussian modulated sine-wave pulse incident on the tissue,

$$H(k) = k^2 \frac{i}{2} \Big[\exp\{-(k + k_0)^2 \sigma_h^2/2\}$$
$$- \exp\{-(k - k_0)^2 \sigma_h^2/2\} \Big] \ , \tag{3}$$

where k_0 is the center frequency of the pulse and σ_h defines the duration of the pulse. Equation (3) combines the response of the measurement system with the reflectivity properties of the medium; the latter is contained in the multiplicative factor k^2.

The objective is to estimate scatterer sizes D from the echo data $X(k)$ for each pixel in the image. Although there is a linear relationship between $X(k)$ and $R(k)$, the relationship between $R(k)$ and D is nonlinear, as seen from (2). Consequently, our estimator is designed to first determine an estimate of the tissue function $\hat{R}(k)$, and then determine the scatterer size estimate $\hat{D}$. Specifically, (2) is used to generate a family of modeled tissue functions $\{Rm(k)\}$ for the range of possible D. Comparing $\{Rm(k)\}$ to $\hat{R}(k)$ using regression analysis, we select $\hat{D}$ from the model function $Rm(k)$ that yields the minimum mean-squared error (MSE). This two-step approach simplifies the analysis considerably because of the linear relationship that exists between $X(k)$ and $R(k)$.

In the next section a MAP estimator of the tissue response is developed. Prior knowledge about $R(k)$, in the form of a probability density function (PDF), is used to estimate $\hat{R}(k)$.

III. MAXIMUM A POSTERIORI (MAP) ESTIMATOR

The posterior conditional probability density of $R(k)$ given the measurement $X(k)$ is $p(R|X)$, and is described by Bayes' formula:

$$p(R \mid X) = \frac{p(X \mid R)p(R)}{p(X)} \ , \tag{4}$$

where $p(X \mid R)$ is the likelihood of the measurement given a specific tissue function, and $p(R)$ and $p(X)$ are the density functions for the tissue and measurement, respectively. The likelihood function describes information about the tissue available from the data at frequency k. $p(R)$ represents the accumulated knowledge of the tissue before data were acquired, and therefore is known as the "prior." It is important to note that R is stochastic in this approach. Stochastic properties of the measurements are represented by $p(X)$. It is reasonable to assume that $p(X)$ is independent of R, since the measurement process is independent of the object. This scaling factor is necessary to give $p(R|X)$ the properties of a density function, but otherwise does not affect the estimator.

Depending on the choice of the cost function, different points on the posterior PDF may be selected to obtain the desired estimate [17]. A popular choice is the mode of the posterior PDF. The corresponding estimator is known as the MAP estimator since it selects solutions that maximize the posterior probability. Similarly, choosing the mean value results in the minimum MSE estimator. For Gaussian or other symmetric density functions, choosing the mean, median, or mode yields the same estimate. ML estimates are obtained by setting $p(R)$ to be constant with respect to R, indicating unavailability of any prior information. In that situation $p(R \mid X) \propto p(X \mid R)$.

An expression for the MAP estimate of the tissue response is obtained from (4) by specifying three important density functions[1]:

$$
\begin{aligned}
p(N) &= \mathcal{N}(0, \sigma_n^2) &&\text{(noise)} \\
p(X|R) &= \mathcal{N}(\overline{X}, \sigma_x^2) &&\text{(likelihood)} \quad (5) \\
p(R) &= \mathcal{N}(\overline{R}, \sigma_R^2) &&\text{(prior)}
\end{aligned}
$$

From (1), $\overline{X} = HR$ is the measurement averaged over the noise ensemble for a fixed object and $\overline{R}$ is the ensemble average of the tissue function. As shown below,

---

[1]In our model, R is real and even, and H is imaginary and odd. Consequently, X is imaginary and the Gaussian likelihood and prior density functions given by (5) are appropriate. However, if the ultrasonic attenuation in the scattering medium is significant, then R and X are complex quantities, and the corresponding likelihood and prior density functions involve circular Gaussian statistics [22]. Kay [17] shows that the MAP and CLS estimators for the corresponding complex quantities are analogous to those for purely real or purely imaginary quantities.

prior information about the object is incorporated into the analysis through $\overline{R}$. Since the noise and object are uncorrelated, σ_x^2 and σ_n^2 are equal, and are independent of k. However, the finite size of the scatterers implies that the power spectral density of the object function is not white, i.e., $\sigma_R^2 \equiv \sigma_R^2(k)$.

Combining the negative logarithm of (4) with (5), we find that, for each k,

$$-\log p(R \mid X) = \frac{1}{2\sigma_n^2}(X - HR)^*(X - HR)$$
$$+ \frac{1}{2\sigma_R^2}(R - \overline{R})^2 + \log p(X) , \quad (6)$$

where $*$ denotes complex conjugate of the quantity. Each quantity in (6) is a function of frequency except σ_n^2.

The MAP estimator is obtained by differentiating (6) with respect to R and setting the result equal to zero. After algebraic manipulation, the MAP estimate for real R can be shown to be

$$\hat{R}_{MAP}(k) = \frac{H^*(k)X(k) + \gamma_{MAP}(k)\overline{R}(k)}{H^*(k)H(k) + \gamma_{MAP}(k)} , \quad (7)$$

where $\gamma_{MAP}(k) = \sigma_n^2/\sigma_R^2(k)$ can be interpreted as the inverse of an input SNR at each frequency, i.e., $[\mathrm{SNR}(k)]^{-1}$. This quantity determines how much weight should be given to the prior at each frequency in the measurement bandwidth. In practice, we use $\gamma_{MAP}(k) = c_1 \hat{\sigma}_n^2/\hat{\sigma}_R^2(k)$, since often only *estimates* of the variances are available. The constant c_1 is introduced to add flexibility in optimizing the estimates for a specific application and to assign a degree of confidence to the model used to estimate γ_{MAP} and the prior. Currently we assume a single γ_{MAP} function for the entire image. However, if information about variation of object properties in the (x, y) image plane is available, then $\gamma_{MAP}(x, y, k)$ may be used in place of $\gamma_{MAP}(k)$ in (7). The advantages of using flexible priors are discussed in two excellent papers by Hanson [23],[24].

The two terms in the numerator of (7) can be viewed as a force pulling the solution in two directions [25]. As SNR increases, γ_{MAP} is reduced to reflect the high reliability of the measurements. Consequently the MAP estimate is determined primarily by the first term, $\hat{R}_{MAP} \longrightarrow X(k)/H(k)$, which is equivalent to the ML estimator described previously [11]. As SNR decreases, however, γ_{MAP} is increased to reflect the poor reliability of the data and to give the prior more weight, such that the second term dominates the estimate, $\hat{R}_{MAP} \longrightarrow \overline{R}$. In the next section, we obtain a constrained least squares solution and review the strong similarities between the two estimates for Gaussian density functions despite the different underlying assumptions.

IV. Constrained Least Squares (CLS) Estimator

An alternative approach to scatterer size estimation is to assume that the object being imaged is deterministic and obtain a least-squares solution. Prior information about R is incorporated into this method by constraining possible solutions based on this knowledge. The problem then reduces to minimizing a cost function by holding the norm of the difference between the model and the measurement constant, i.e., $\| HR - X \|^2 = $ constant. Choosing the norm of the error between a prior guess $\overline{R}$ and the true estimate R as the cost function, $\| R - \overline{R} \|^2$, and using the linear model specified by (1), the minimization problem can be restated as

$$R = \arg\min_R \ (HR - X)^*(HR - X)$$
$$+ \gamma_{CLS}(R - \overline{R})^*(R - \overline{R}) , \quad (8)$$

where γ_{CLS} is the Lagrangian multiplier that indicates the relative degree of confidence between the measurements and the prior. We differentiate the functional defined in (8) with respect to R, set the result to zero, and simplify to find the CLS estimate of R:

$$\hat{R}_{CLS}(k) = \frac{H^*(k)X(k) + \gamma_{CLS}(k)\overline{R}(k)}{H^*(k)H(k) + \gamma_{CLS}(k)} . \quad (9)$$

As with $\gamma_{MAP}(k)$ in (7), $\gamma_{CLS}(k)$ in (9) determines the weight assigned to prior knowledge relative to the measurement. While a small value of $\gamma_{CLS}(k)$ results in a solution that approaches the least squares (and ML) solution, a large $\gamma_{CLS}(k)$ puts more weight on the prior. Therefore, γ_{CLS} can be adjusted based on the reliability of measurements and the amount of noise. Although several methods for selecting γ_{CLS} have been proposed [19],[26],[27], they usually require solving the inverse problem several times to identify the appropriate value. Since we are most interested in estimators that can be used for high-speed imaging, these approaches are not feasible. Based on characteristics of the object, we chose

$$\gamma_{CLS}(k) = \frac{c_2}{|H(k)|^2} , \quad (10)$$

where c_2 is a constant. Such a function gives more weight to spectral measurements near the center frequency where the measurement is most sensitive ($\mathrm{SNR}(k)$ is large) than at the limits of the bandwidth where the measurement is least sensitive ($\mathrm{SNR}(k)$ is small). This choice of γ_{CLS} closely parallels the definition of γ_{MAP}, since an optimal experimental setup requires that we select a pulse function for $H(k)$ that is well matched to the most sensitive frequencies of the object function $R(k)$.

The CLS and MAP estimators are identical except for the weighting function γ, although the physical models of the object for the two approaches are very different. In the MAP estimate, γ_{MAP} appears naturally as a quantity estimated from knowledge of noise and object statistics. In the CLS estimate, we have selected γ_{CLS} to be inversely proportional to the sensitivity function. For γ_{MAP} and γ_{CLS} used in this work, MAP and CLS techniques yield estimates that are numerically equivalent. The similarity of the two estimates is a consequence of R having a Gaussian distribution. In general, the two approaches do not yield the same estimator.

It is also possible to generate an estimator that smooths the result without prior information about the average object function $\overline{R}(k)$. Setting $\overline{R}(k) = 0$ in (7) and (9) gives

$$
\begin{aligned}
\hat{R}_{Wiener}(k) &= \frac{H^*(k)}{H^*(k)H(k) + \gamma(k)} X(k) \\
&= A(k)X(k) \ ,
\end{aligned}
\tag{11}
$$

where $A(k)$ is the Wiener filter [17],[18].

For high noise levels, it is best to apply the CLS technique iteratively; gradually introducing the information from the data at successive iterations results in a higher contrast-to-noise ratio compared to a single iteration. At the first iteration, we use $\overline{R}$ for the prior to obtain $\hat{R}$, as in (9). The first estimate is then used in place of $\overline{R}$ to form an updated estimate, and the process is continued until there is no further improvement in the quality of the estimate. The general iteration scheme can be represented as:

$$
\hat{R}_{CLS}^{\ell+1}(k) = \frac{H^*(k)X(k) + \gamma_{CLS}^{\ell}(k)\hat{R}_{CLS}^{\ell}(k)}{H^*(k)H(k) + \gamma_{CLS}^{\ell}(k)}
$$
$$
\text{for } \ell = 0, 1, 2, \ldots
\tag{12}
$$

where $\hat{R}_{CLS}^{\ell} = \overline{R}$ for $\ell = 0$. Only c_2, (10), is varied with each γ_{CLS}^{ℓ}. It is intentionally set to a value larger than the optimal value for the initial iteration, and is gradually decreased for successive iterations. The number of iterations required depends on SNR, but ultimately, the success of this technique is determined by the choice of c_2 at each iteration.

The iterative scheme presented here is similar to Picard's iterations that are known to work well only if the initial estimates are close to the true values [16]. In our application, reasonably accurate priors are available, so that the iterative method of (12) could provide a distinct computational advantage over other more complex techniques [28]. Evidence in support of this hypothesis is provided in Section VI.

V. ALGORITHM PERFORMANCE

The performance of the above estimators are compared for the task of discriminating among regions of differing scatterer size. Normally, the best estimators are unbiased and yield minimum variance [17]. Our task, however, is one of detection, to maximize the visibility of targets in scatterer size images. To minimize variance, we are willing to introduce some bias as long as sufficient dynamic range is preserved. Therefore, the performance criterion is chosen to be the contrast-to-noise ratio defined as:

$$
\begin{aligned}
\text{CNR} &= \frac{\left(\overline{\Delta \hat{D}}\right)^2}{\text{var}(\Delta \hat{D})} \\
&= \frac{(\overline{\hat{D}_i} - \overline{\hat{D}_j})^2}{\text{var}(\hat{D}_i) + \text{var}(\hat{D}_j)} \ ,
\end{aligned}
\tag{13}
$$

Fig. 1. Simulated phantom used for the investigation. The object consists of a background region with $\bar{D} = 100$ μm, an outer cortical ring with $\bar{D} = 200$ μm, an inner medullary ring with $\bar{D} = 50$ μm, and a central circular region with $\bar{D} = 75$ μm.

where i, j indicate two regions with mean scatterer size estimates $\overline{\hat{D}_i}$ and $\overline{\hat{D}_j}$ and variances $\text{var}(\hat{D}_i)$ and $\text{var}(\hat{D}_j)$, respectively. In our study, the C-scan pixels are uncorrelated, therefore $\text{cov}(\hat{D}_i, \hat{D}_j) = 0$. CNR indicates how well two regions of the image can be distinguished visually but does not account for the existence of a bias that affects the two regions equally. The mean squared error MSE = $\text{var}(\Delta \hat{D}) + \text{bias}^2(\Delta \hat{D})$ does include the effects of bias but does not address our detectability task. We use CNR to assess algorithm performance, but if the bias is known, the two measures may be related according to CNR = $\left[\text{MSE} + (2\overline{\Delta \hat{D}\Delta D} - \overline{\Delta D}^2)\right] /\text{var}(\Delta \hat{D}) - 1$.

VI. RESULTS

Several simulations were performed to investigate the effect of prior information on task performance. A 128×128-pixel C-scan data set of echo signals from a kidney was simulated for the investigation. This software phantom had four regions that differed in average scatterer size: a background region with $D = 100 \pm 15$ μm, an outer elliptical ring with $D = 200 \pm 25$ μm to simulate scatterers in the renal cortex, an inner region with $D = 50 \pm 10$ μm to simulate scatterers in the renal medulla, and a central circular region with $D = 75 \pm 15$ μm. The ensemble mean of the object function is depicted in Fig. 1.

A sampling rate of 25 MHz and a center frequency of 5 MHz were used for the simulations. The Gaussian pulse duration was determined by $\sigma_h = 0.1125$ μs (3), which gave a full-width-at-half-maximum amplitude bandwidth of 3.33 MHz (67%) before adding noise. Performance of the estimator was investigated as a function of the echo waveform SNR ((11) in [12]) and range gate duration. The former indicates the relative amount of noise power added to the echo data and the latter indicates image slice thickness. The measurement bandwidth was 60% for high SNR (20 dB), and 40% for low SNR (5 dB).

An ML reconstruction of the object depicted in Fig. 1 using a periodogram-based estimator (henceforth referred to as ML) is shown in Fig. 2a for a 256-point waveform and 20 dB SNR. This is the technique we currently use for scatterer size imaging [6],[11]. For the same echo data, the image in Fig. 2b was obtained with the MAP/CLS algorithm, (7) or (9). Since $\gamma_{CLS} = \gamma_{MAP} \equiv \gamma$, the CLS result is equivalent to the MAP result for a single iteration, $\ell = 1$. Those images are labeled MAP/CLS. However, images obtained from (12) for $\ell > 1$ are labeled CLS. The image of Fig. 2b was formed with a single iteration because, at high SNR, more iterations produced no further improvements in CNR. The prior information used to form Fig. 2b was $\overline{D} = 100$ μm. $\overline{R}(k)$ in (9) was obtained from (2), assuming $\overline{D} = 100$ μm for the entire image. Therefore, the prior information was not entirely accurate throughout the image, and no information about the shape of the object was used.

The effect of reducing the SNR on algorithm performance was also investigated. The image obtained for data at 5 dB SNR with the ML algorithm is shown in Fig. 2c. For the same prior information ($\overline{D} = 100$ μm), the reconstruction with three iterations of the CLS technique is depicted in Fig. 2d.

An image obtained using the Wiener filter estimator of (11) is shown in Fig. 2e, and the result of the CLS estimator when γ is independent of frequency is shown in Fig. 2f. In both images, the SNR was 5 dB and the values for γ were adjusted to give the highest CNR performance.

A similar set of simulations was performed with 32-point echo waveforms. The information content per echo waveform was proportionately lower for these cases. At 20 dB SNR, reconstructions with ML and two iterations of the CLS technique are shown in Fig. 3a and b, respectively. The corresponding images for 5 dB SNR are shown in Fig. 3c and d. Although overall brightness was adjusted to achieve the same average background brightness for each image, the contrast was not altered.

Finally, values for CNR and average scatterer size estimated in the cortex and medulla regions are listed in Table I. Comparing the values of $\hat{D}$ with the object values $\overline{D}$ (200 μm cortex, 50 μm medulla) indicates the amount of bias each algorithm produces and how that bias influences performance.

VII. Discussion

The effects of speckle and additive (electronic and digitization) noise are apparent even for long waveform duration, high SNR data segments. The performance (CNR) achieved with the CLS algorithm is more than eight times that for the ML estimate at 20 dB SNR although the prior information only coarsely approximates the object. For the same set of experimental conditions, but with no additive noise, we calculated the theoretical performance limit for the unbiased ML algorithm [12] to be CNR $\times$ 100 = 492.56. The CLS algorithm exceeds this limit by more than a factor of five by smoothing and biasing the estimates (Table I). Thus, the high CNR value for the CLS

result of Fig. 2b is achieved at the cost of a reduced dynamic range.

At low SNR, the CLS algorithm provided its most significant improvement in task performance through multiple iterations, where the information from the data is gradually introduced into the solution. At 5 dB SNR, the ML reconstruction is very noisy, as seen in Fig. 2c. The improved quality of the image in Fig. 2d is due to a large decrease in variance when the smooth prior is used. For the task we defined, the large negative bias in the CLS estimates is not a limitation since the objective is to suppress the noise while preserving contrast.

The advantage of the iterative CLS approach may be understood by examining Fig. 4, where CNR $\times$ 100 is plotted as a function of c_2. For one iteration ($\ell = 1$ in (12)), $c_2 = 0.1$ gives the best performance. The result at $c_2 = 0$ corresponds to the ML solution, and at $c_2 = \infty$ corresponds to the solution as given by the prior where $\Delta\overline{D} = 0$. For multiple iterations, however, we find it best to set $c_2 > 0.1$ at the first iteration, which oversmooths the solution, and to gradually decrease c_2 at subsequent iterations. Using $\hat{R}_{CLS}^{\ell=1}(k)$ as the prior for the $\ell = 2$ iteration gives a CNR that is nearly doubled. A third iteration produces additional improvement in peak CNR, but for $\ell \geq 4$ performance is essentially unchanged. Iterations do not increase CNR unless c_2 is set to be greater than the value at the peak. If it is much greater, then many iterations are needed to reach the same peak performance. Slightly oversmoothing the estimate by setting $c_2 > 0.1$ in our example uses only a portion of the information contained in the data at the first iteration. Updating the prior with the $\ell = 1$ estimate uses a smoothed version of the data for $\overline{R}$ for the $\ell = 2$ estimate. The new prior is more accurate but less smooth than the first prior. Iteration balances the need for a smooth result with the need for an accurate result. The bias-variance tradeoff inherent in the CLS estimator is complicated by the nonlinear nature of the estimate.

The MAP/CLS method uses the prior to minimize estimation bias. If the prior is accurate, CLS estimation bias is zero. The Wiener filter result of Fig. 2e uses $\overline{R} = 0$; prior knowledge is used only to determine the degree of smoothness in the estimate. Therefore γ must be kept small to avoid very high bias and loss of dynamic range. Low values of γ smooth the estimates and reduce variance very little, so the CNR is not improved appreciably over the ML result. Similarly, setting γ_{CLS} to a constant, as in Fig. 2f, we ignored prior information about how noise varies with frequency, and consequently we found little improvement in performance. While constant γ is frequently used for simplicity, in this application the addition of the frequency information was valuable. The advantages of using prior information are obvious from Fig. 3 where the image slice thickness is reduced from 256 points (7.9 mm) to 32 points (1.0 mm).

In all the images of Figs. 2 and 3, the central circular region with $\overline{D} = 75$ μm is lost. The lack of contrast in this region is more a consequence of reduced sensitivity at the center frequency for those scattering structures rather than a noise limitation [11],[12]. At 5 MHz, the echo
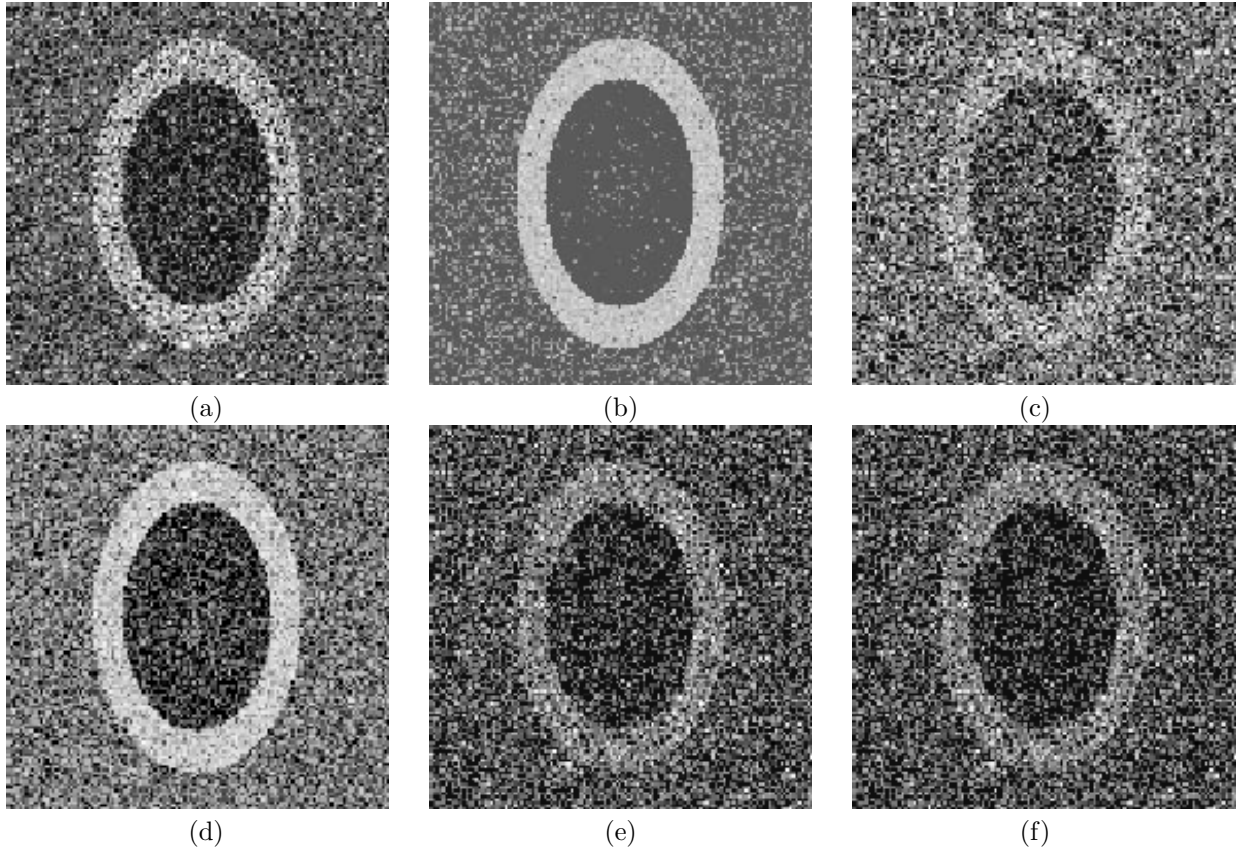
Fig. 2. Images obtained for a C-scan data set consisting of 128 × 128 echo waveforms, each 256-points in duration (7.9 mm slice thickness). (a) ML and (b) MAP/CLS algorithms obtained at 20 dB SNR; (c) and (d) are corresponding images at 5 dB SNR with $\ell = 3$ in (d); (e) is the image obtained with the Wiener filter for 5 dB SNR; and (f) is the MAP/CLS algorithm for 5 dB SNR when γ_{CLS} is constant.

TABLE I

CNR AND $\overline{D}$ FOR MEDULLA AND CORTEX REGIONS FOR VARIOUS SIMULATIONS (SEE FIG. 1).

N	SNR	Technique	CNR×100	$\overline{\hat{D}}_{medulla}$	$\overline{\hat{D}}_{cortex}$
256	20 dB	ML-Periodogram	314.48	61.31	206.08
		CLS/MAP	2721.07	15.75	102.86
	5 dB	ML-Periodogram	86.87	92.49	183.64
		CLS	254.95	22.42	93.03
		CLS (γ const.)	94.11	56.04	134.55
		Wiener Filter	95.14	59.41	138.16
32	20 dB	ML-Periodogram	51.16	83.80	181.19
		CLS	245.67	31.16	144.40
	5 dB	ML-Periodogram	1.01	130.71	148.33
		CLS	9.47	63.08	105.42

spectrum is most sensitive to variations in $\overline{D}$ near 100 μm because the product of wave number and scatterer radius $kD/2$ is approximately 1. In the central medullary region where $\overline{D} = 50$ μm, the target is made visible by increasing the center frequency to 8 MHz, (Fig. 5). The ML algorithm was used to process 256-point echo waveform data at 20 dB SNR for the same test object. Although the central target is now clearly visible, the contrast between the bright cortical region and the background is significantly degraded since $ka \approx 3.3$ in that region.

An inherent limitation of techniques that use prior information in estimation is that they bias the estimate based on the prior and the choice of γ. Therefore, in the absence of accurate prior knowledge, the MAP/CLS technique does not improve performance and may further degrade the image. Accurate priors are needed the most when the dynamic range of the estimator is limited. In that case, autoregressive (AR) spectral estimation methods, used in conjunction with the ML algorithm [29], offer significant advantages.

The periodogram-based ML estimator can also be biased if the data segment is too short. To keep distortion of the echo spectra less than 2%, the system bandwidth B_g must exceed the spectral resolution B_r by a
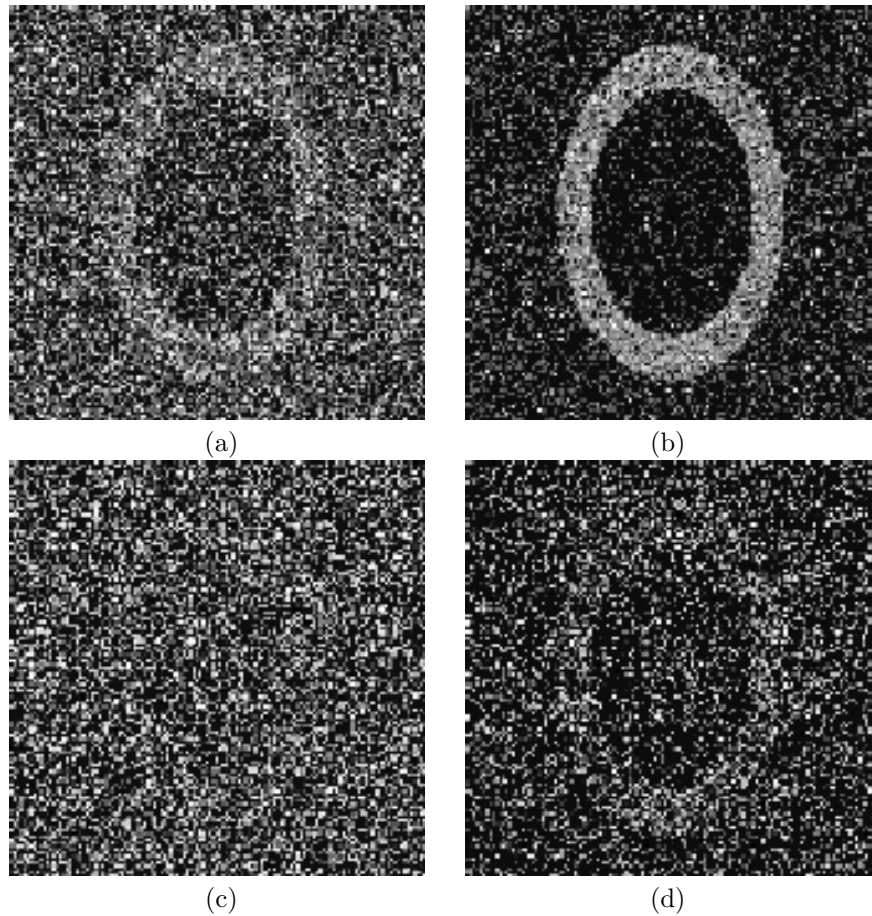
Fig. 3. Images obtained for a 32-point segment (1.0 mm slice thickness). (a) ML and (b) CLS reconstructions obtained at 20 dB SNR; (c) and (d) are corresponding images at 5 dB SNR.
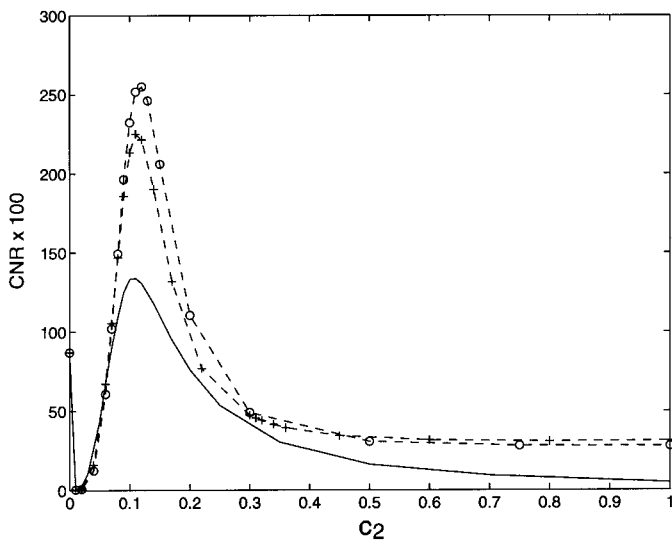

Fig. 4. Contrast-to-noise ratio (CNR) obtained with iterative CLS technique for a 256-point segment at 5 dB SNR. Solid line: 1 iteration; $-+-$: 2 iterations; $-\circ-$: 3 iterations. The ML estimate corresponds to $c_2 = 0$.
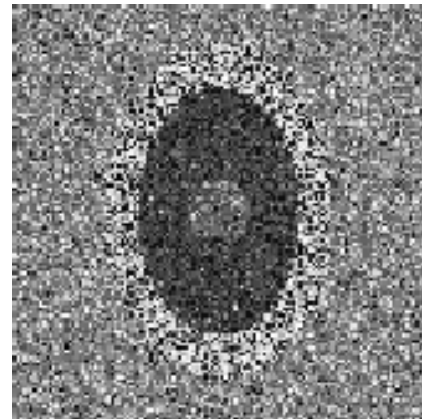

Fig. 5. ML reconstruction of the test object for a 256-point echo signal at 20 dB SNR when the transducer center frequency is 8 MHz and nominal bandwidth is 60%.

factor of four [30], where B_r along the beam axis is determined by the duration of the windowed data segment. Using (30) from [31] and the experimental parameters defined in Section VI, we estimated the 3 dB spectral resolution: $B_r \simeq 37.04/N$ cycles/mm, where N is the number of data points in the waveform segment. The relation between the duration of our rectangular window T and that

of the Gaussian-weighted window, α_t in [31], is $T = \sqrt{\pi}\alpha_t$, which is found by comparing the equivalent bandwidths [32]. The 3 dB system bandwidth for the Gaussian pulse is $B_g \simeq 3.06$ cycles/mm. For the experimental parameters of our simulation, the bias of the ML estimator is less than 2% when $N \geq 48$ points. Analysis of our simulated echo signals confirms that the spectra begin to flatten at a waveform duration of approximately 2 μs. Consequently, the bias in the ML results of Fig. 3a and 3c, and summarized in Table I, are expected. To avoid windowing effects, AR-based ML methods are recommended for thin slice reconstructions [29] when shapes of the pulse and tissue spectra are known.

In real kidneys, small and large scatterers are spatially mixed, a feature that was not simulated in this study. However, the issue was partially addressed by assuming a Gaussian distribution for the object in the development of the MAP estimate in (7). How the distribution of scatterer sizes within a pulse-volume affects the validity of the models used in this work is an important issue that needs to be resolved. As part of future work, we intend to perform several experiments and a detailed analysis to test the reliability of the results obtained from the simulations.

VIII. Conclusions

Integrating accurate prior information into the estimation process can significantly increase the visibility of targets in scatterer size images. The Bayesian approach is equivalent to a single iteration CLS estimator in our application. The MAP formulation was important for choosing useful regularization functions, γ. For high SNR and/or large slice thicknesses, a single iteration is sufficient, and for low SNR and/or small slice thicknesses, an iterative CLS technique offers significant advantages. Scatterer size estimates obtained with the CLS method are biased when the priors are not exactly accurate. Nevertheless, the large improvement in CNR greatly improves the detectability so important for diagnosis.

References

[1] M. F. Insana, J. G. Wood, and T. J. Hall, "Identifying acoustic scattering sources in normal renal parenchyma *in vivo* by varying arterial and ureteral pressures," *Ultrasound Med. Biol.*, vol. 18, pp. 587–599, 1992.

[2] M. F. Insana, J. G. Wood, and T. J. Hall, "Effects of endothelin-1 on renal microvasculature measured using quantitative ultrasound," *Ultrasound Med. Biol.*, vol. 21, pp. 1143–1151, 1995.

[3] R. L. Romijn, J. M. Thijssen, J. L. van Delft, D. de Wolff-Rouendaal, J. van Best, and J. A. Oosterhuis, "In vivo ultrasound backscattering estimation for tumour diagnosis: an animal study," *Ultrasound Med. Biol.*, vol. 15, pp. 471–479, 1989.

[4] K. A. Wear, M. R. Milunski, S. A. Wickline, J. E. Perez, B. E. Sobel, and J. G. Miller, "Contraction-related variation in frequency dependence of acoustic properties of canine myocardium," *J. Acoust. Soc. Am.*, vol. 86, pp. 2067–2072, 1989.

[5] E. J. Feleppa, F. L. Lizzi, D. J. Coleman, and M. M. Yaremko, "Diagnostic spectrum analysis in ophthalmology: a physical perspective," *Ultrasound Med. Biol.*, vol. 12, pp. 623–631, 1986.

[6] M. F. Insana, T. J. Hall, J. G. Wood, and Z. Y. Yan, "Renal ultrasound using parametric imaging techniques to detect changes in microstructure and function," *Invest. Radiol.*, vol. 28, pp. 720–725, 1993.

[7] F. L. Lizzi, D. L. King, M. C. Rorke, J. Hui, M. Ostromogilsky, M. M. Yaremko, E. J. Feleppa, and P. Wai, "Comparison of theoretical scattering results and ultrasonic data from clinical liver examinations," *Ultrasound Med. Biol.*, vol. 14, pp. 377–385, 1988.

[8] M. F. Insana, "Modeling acoustic backscatter from kidney microstructure using an anisotropic correlation function," *J. Acoust. Soc. Am.*, vol. 097, pp. 649,655, 1995.

[9] F. L. Lizzi, M. Ostromogilsky, E. J. Feleppa, M. C. Rorke, and M. M. Yaremko, "Relationship of ultrasonic spectral parameters to features of tissue microstructure," *IEEE Trans. Ultrason., Ferroelect., Freq. Contr.*, vol. 34, pp. 319–329, 1987.

[10] R. C. Waag, J. O. Nilsson, and J. P. Astheimer, "Characterization of volume scattering power spectra in isotropic media from power spectra of scattering by planes," *J. Acoust. Soc. Am.*, vol. 74, pp. 1555–1571, 1983.

[11] M. F. Insana and T. J. Hall, "Parametric ultrasound imaging from backscatter coefficient measurements: image formation and interpretation," *Ultrasonic Imaging*, vol. 12, pp. 245–267, 1990.

[12] P. Chaturvedi and M. F. Insana, "Error bounds on ultrasonic scatterer size estimates," *J. Acoust. Soc. Am.*, vol. 100, no. 1, pp. 392–399, 1996.

[13] P. Cortes, X. Zhao, F. Dumler, B. C. Tilley, and J. Atherton, "Age-related changes in glomerular volume and hydroxyproline content in rat and human," *J. Am. Soc. Nephrology*, vol. 2, pp. 1716–1725, 1992.

[14] Y. Yoshida, T. Kawamura, M. Ikoma, A. Fogo, and I. Ichikawa, "Effects of antihypertensive drugs on glomerular morphology," *Kidney International*, vol. 36, pp. 626–635, 1989.

[15] K. M. Hanson, "Bayesian and related methods in image reconstruction from incomplete data," in *Image Recovery: Theory and Application*, ed. H. Stark. Orlando: Academic Press, 1987, pp. 79–125.

[16] B. R. Hunt, "Bayesian methods in nonlinear digital image restoration," *IEEE Trans. Computers*, vol. C-26, pp. 219–229, 1977.

[17] S. M. Kay, *Fundamentals of Statistical Signal Processing: Estimation Theory*, Englewood Cliffs, NJ: Prentice Hall, 1993.

[18] R. C. Gonzalez and P. Wintz, *Digital Image Processing*, 2nd. ed. Reading, MA: Addison-Wesley, 1987.

[19] A. E. Hoerl and R. W. Kennard, "Ridge regression: biased estimation for nonorthogonal problems," *Technometrics*, vol. 12, pp. 55–67, 1970.

[20] D. W. Marquardt and R. D. Snee, "Ridge regression in practice," *The American Statistician*, vol. 29, pp. 3–20, 1975.

[21] S. Twomey, *Introduction to the Mathematics of Inversion in Remote Sensing and Indirect Measurements*, Elsevier Scientific Publishing, New York, 1977.

[22] R. F. Wagner, S. W. Smith, S. J. M. Sandrik, and H. Lopez, "Statistics of speckle in ultrasound B-scans," *IEEE Trans. Sonics and Ultrason.*, vol. 30, no. 3, pp. 156–163, 1983.

[23] K. M. Hanson, "Reconstruction based on flexible prior models," *Proc. SPIE*, vol. 1652, pp. 183–191, 1992.

[24] K. M. Hanson, "Bayesian reconstruction based on flexible prior models," *J. Opt. Soc. Am. A*, vol. 10, no. 5, pp. 997–1004, 1993.

[25] S. Geman and D. Geman, "Stochastic relaxation, Gibb's distributions, and Bayesian restoration of images," *IEEE Trans. Pattern Anal. Machine Intell.*, vol. PAMI-6, pp. 721–741, 1984.

[26] N. P. Galatsanos and A. K. Katsaggelos, "Methods for choosing the regularization parameter and estimating the noise variance in image restoration and their relation," *IEEE Trans. Image Proc.*, vol. 1, pp. 322–336, 1992.

[27] D. W. Marquardt, "Generalized inverses, ridge regression, biased linear estimation, and nonlinear estimation," *Technometrics*, vol. 12, pp. 591–612, 1970.

[28] J. L. Buchanan and P. L. Turner, *Numerical Methods and Analysis*, New York: McGraw-Hill, 1992.

[29] P. Chaturvedi and M. F. Insana, "Autoregressive spectral estimation in ultrasonic scatterer size imaging," *Ultrasonic Imaging*, vol. 18, pp. 10–24, 1996.

[30] J. S. Bendat and A. G. Piersol, *Random Data: Analysis and Measurement Procedures,* 2nd ed. New York: Wiley, 1986, p. 282.

[31] T. D. Mast and R. C. Waag, "Wave space resolution in ultrasonic scattering measurements," *J. Acoust. Soc. Am.,* vol. 98, pp. 3050–3058, 1995.

[32] K. S. Shanmugan and A. M. Breipohl, *Random Signals: Detection, Estimation and Data Analysis*, New York: Wiley, 1988, p. 147.

Pawan Chaturvedi (S'91,M'92,S'93,M'95) was born in Katni, India on January 21, 1968. He received the B.Sc. (Honors) degree in physics from the University of Delhi in 1988, M.Sc. in physics from the Indian Institute of Technology, Delhi in 1990, M.S. in electrical engineering from Tulane University, New Orleans in 1992, and a Ph.D. in electrical engineering from the University of Kansas in 1995. During the summer of 1989, he was a visiting researcher at the Tata Institute of Fundamental Research, Bombay. From 1990 to 1995 he held teaching and research assistant positions at Tulane University and the University of Kansas. Since 1995, he has been a research associate in the Department of Radiology at the University of Kansas Medical Center in Kansas City. His research interests are primarily in the fields of inverse problems, acoustic and electromagnetic imaging, and signal and image processing. He is a member of Tau Beta Pi, Eta Kappa Nu, and Phi Beta Delta.

Michael F. Insana (M'85) was born in Portsmouth, VA on December 18, 1954. He received the B.S. degree in physics from Oakland University, Rochester, MI in 1978 and the M.S. and Ph.D. degrees in medical physics from the University of Wisconsin, Madison, WI in 1982 and 1983, respectively. From 1984 to 1987 he was a research physicist at the FDA's Center for Devices and Radiological Health, where he worked in medical imaging with emphasis on acoustic signal processing. He is currently Associate Professor of Radiology at the University of Kansas Medical Center. His current research interests are acoustic imaging and tissue characterization, signal detection and estimation, observer performance measurements, and image quality assessment. He is a member of the IEEE, SPIE, ASA, AIUM, and AAPM professional societies.